Characterisation of the HDRF (as a proxy for BRDF) of snow surfaces at Dome C, Antarctica, for the inter-calibration and inter-comparison of satellite optical data

Amelia Marks[a], Corrado Fragiacomo[b], Alasdair MacArthur[c], Giuseppe Zibordi[d], Nigel Fox[e], Martin D. King[a,*]

[a]*Department of Earth Sciences, Royal Holloway University of London, Egham, Surrey, TW20 0EX, UK*
[b]*National Institute of Oceanography and Geophysics, 1-34100, Trieste, Italy*
[c]*NERC Field Spectroscopy Facility, GeoSciences University of Edinburgh, Edinburgh, EH9 3JW, UK*
[d]*European Commission, Joint Research Centre, I-21027 Ispra (VA), Italy*
[e]*National Physical Laboratory, Hampton Road, Teddington, Middlesex, TW11 0LW, UK*

Abstract

Measurements of the Hemispherical Directional Reflectance Factor (HDRF) of snow surfaces were performed at Dome C, Antarctica, during the Australis Summer 2011–2012 to support the inter-comparison and intercalibration of satellite optical sensors. HDRF data were collected with the Gonio Radiometric Spectrometer System (GRASS) which performs hyper-spectral measurements of radiance from the same target surface with independent collectors at a number of viewing and azimuth angles in the 0–60° and 0–360° angular ranges, respectively. The radiance collectors, installed on a hemispheric frame and connected to a spectrometer through fibre optics, have an 8° full cone of acceptance and a viewing footprint varying from 0.049 m^2 at nadir to 0.142 m^2 at viewing angles of 60°. These relatively small footprints allow for the characterisation of small-scale heterogeneities in the HDRF of observed surfaces. HDRF measurements representative of the Dome C snow surfaces were made at eight different sites along a transect approximately 100 m long. All the sites exhibit similar

___

*Corresponding author
Email address:* `m.king@es.rhul.ac.uk` (Martin D. King)

HDRF distributions with inter-site differences explained by small-scale inhomogeneities of the surface. The measured HDRF display marked forward scattering with anisotropy increasing with wavelength in the 400–1600 nm spectral region. These data complement those from previous measurements performed in the same area with a different technique. Agreement between the two data sets is shown by differences generally lower than 4% between HDRF distributions derived from a previous study and the spatially averaged HDRF from the various sites along a transect presented in this work.

1. Introduction

Measurements of planetary albedo are crucial to quantify the global energy budget, which determines Earth's weather and climate (e.g. Trenberth et al. (2009); Kiehl & Trenberth (1997)). Planetary albedo can be determined from remote sensing observations using satellite optical sensors. These satellite data products generally consist of measurements of the surface radiance performed with narrow field-of-view over limited viewing angles during successive orbits from space. These radiance measurements are converted into albedo by assuming the bi-directional reflectance distribution function (BRDF) of a surface, which describes the surface reflectance as a function of viewing and illumination geometries, is known.

Long-term observations of planetary albedo are essential for climate studies aiming at detecting small changes embedded in large seasonal and inter-annual variations. The application of Earth Observation techniques to investigate climate changes over decadal periods, requires the combination of remote sensing data from successive missions and different sensors. Thus, the intercalibration of sensors applied for climate applications is a fundamental necessity to avoid introducing inconsistencies in time-series, which may mask climate effects (Fox et al., 2011). The inter-calibration of space sensors can be performed using observations of stable natural targets with the different space sensors. In both

2

cases, information on the surface BRDF is fundamental to account for different viewing and illumination geometries determining the radiance measured from space.

Deserts and permanent snow fields are often used as natural calibration sites as they are spatially homogeneous, temporally stable and efficient reflectors (e.g. Angal et al. (2011); Masonis & Warren (2001)). Early measurements documenting the anisotropic reflectance of snow surfaces were performed in the early 1950s by Middleton & Mungal (1952). These were then followed by successive investigations (see (Warren, 1982)) which showed the marked forward scattering of snow and the BRDF dependence on grain size (e.g. Kuhn (1985); Dozier et al. (1988); Aoki & Fukabori (2000); Painter & Dozier (2004); Peltoniemi et al. (2005)). Geometrical features of the snow surface were also shown to have an important effect on measured BRDF at different spatial resolutions, e.g. sastrugi (Warren et al., 1998) and surface roughness (Peltoniemi et al., 2005). Snow BRDF has also been measured at several localities using different techniques (e.g. Warren et al. (1998); Hudson et al. (2006); Aoki & Fukabori (2000); Painter & Dozier (2004); Peltoniemi et al. (2005)). BRDF of snow was additionally determined under laboratory conditions (Dumont et al., 2010) and through modelling (e.g. Leroux et al. (1999); Dozier et al. (1988)).

Dome C, Antarctica (75°S, 123°E) was suggested as an excellent ground-calibration site for measurement of the BRDF (Six et al., 2004) as the surface is relatively flat (Rémy et al., 1999) and spatially homogeneous, with weak surface roughness owing to wind effects (Gallet et al., 2011), leading to the formation of sastrugi less than 10–20 cm (Petit et al., 1982). Additionally the snow surface at Dome C is not influenced by the underlying terrain and is relatively stable with time due to a small snow accumulation rate and low winds (Keller et al., 2002). Owing to the high altitude (> 3000 m) and its long distance from the coast (>1000 km) the atmospheric conditions of Dome C favour clear skies with very low column aerosol and a small atmospheric water vapour content (e.g. Six et al. (2005)). Finally, and importantly for the inter-calibration and inter-comparison of Earth Observation sensors, the area is frequently revisited by Polar orbiting

3

Earth Observation sensors.

Hudson et al. (2006) previously took measurements of BRDF at Dome C from the top of a 32 m tower. These measurements were performed in the 350–2400 nm spectral interval and were reported as distributions of the "anisotropic reflectance factor". Each observation sequence involved 85 independent and successive measurements of the surface radiance from the snow surface at viewing angles from 22.5 to 82.5° and azimuth angles from 142.5° to 37.5°. These measurements clearly show forward scattering increasing with wavelength and also anisotropy values lower for a roughened than for a flat snow surface. The comprehensive study of Hudson et al. (2006) was limited by methodological constrains: (i.) the impossibility of performing measurements at viewing angles lower than 22.5°; (ii.) restrictions in the range of azimuth angles (142.5° to 37.5°); (iii.) the need of observing different snow targets for each different azimuth/viewing angle. The last constraint, (iii), imposes the assumption of homogeneous properties for the whole measurement area: a condition duly supported by the use of a large viewing footprint varying from approximately 70 m^2 at viewing angles of 22.5° up to 1170 m^2 at 82.5°.

The objective of this work is to present new angular reflectance measurements of the snow surface at Dome C performed by using a methodology relying on simultaneous measurements of the same target surface with relatively small viewing footprints (i.e., varying from 0.049 to 0.141 m^2) and all azimuth angles, overcoming limitations ii and iii. A small viewing footprint enables small scale ($<< 1$ m) inhomogeneities in Dome C snow surface to be observed, which is potentially important for future high spatial resolution sensors with a ground sample distance (GSD) of less than 1 m (Jacobsen, 2005), and also has important uses for inputs into radiative transfer models. Spatial averaging of multiple HDRF measurements completed with a small viewing footprint also produces HDRF values that are representative of current typical satellite sensor resolutions (with a GSD of 10–100 m), thus the values can also be utilised for current satellite calibration. Measurements at Dome C were performed using the Gonio Radiometric Spectrometer system (GRASS) shown in Figure 1 and presented

4

in section 3.3. The measurements applied in this work were made with 1 nm spectral resolution in the 400–1700 nm spectral region over viewing angles from nadir to 60° and azimuth angles regularly distributed over 360°.

2. Reflectance terminology

BRDF, see Figure 2, is the ratio of radiance reflected at a known viewing and relative azimuth angle to incident light intensity at a known zenith angle, θ_i over a hemisphere (Nicodemus et al., 1977). The BRDF of a surface cannot be measured in the field as it is an infinitesimal quantity requiring determination of incident light from one, infinitesimally small, solid angle and that reflected from a infinitesimally small, solid angle. An alternative quantity which does not require measurement of incoming radiation is the bidirectional reflectance factor (BRF) which defines the ratio of radiance reflected from the target surface to the reflected radiance from an ideal (Lambertian) reflector under identical illumination and viewing geometries (Schaepman-Strub et al., 2006; Nicodemus et al., 1977). However BRF is still defined with infinitesimal reflected solid angles which makes it as conceptual as BRDF. BRF is defined by equation 1, where, Φ_r is the radiance of the target surface and Φ_r^{id} is the radiance of an ideal (Lambertian) surface (Schaepman-Strub et al., 2006). The Lambertian properties of an ideal surface allow θ_r and ϕ_r in Equation 1 to be omitted.

$$BRF(\theta_i; \theta_r, \phi_r) = \frac{d\Phi_r(\theta_i; \theta_r, \phi_r)}{d\Phi_r^{id}(\theta_i; \theta_r, \phi_r)} = \frac{d\Phi_r(\theta_i; \theta_r, \phi_r)}{d\Phi_r^{id}(\theta_i)} \tag{1}$$

The hemispherical-directional reflectance factor (HDRF) is similar to BRF but is determined using the irradiance from the whole downward hemisphere (direct and diffuse solar radiation) and thus it is dependent on atmospheric conditions and reflectance from the local surrounding area (Schaepman-Strub et al., 2006), see equation 2.

$$HDRF(\theta_i, 2\pi; \theta_r, \phi_r) = \frac{\Phi_r(\theta_i, \phi_i, 2\pi; \theta_r, \phi_r)}{\Phi_r^{id}(\theta_i, 2\pi)} \tag{2}$$

As wavelength increases the contribution of diffuse irradiance to total irradiance greatly decreases, thus measurements of the HDRF of snow at wavelengths greater than 800 nm are not significantly influenced by diffuse light (Li & Zhou, 2004). HDRF is therefore a convenient estimate of BRF in the near-infrared part of the spectrum, under natural observation conditions. In the study presented here the quantity that has been measured is strictly, according to Schaepman-Strub et al. (2006), a Hemispherical Conical Reflectance Factor (HCRF) since the reflected radiance is measured conically, not directionally. HCRF approximates to HDRF, for a small solid angle of a viewing optic and to keep in concordance with common terminology the term HDRF will be used to describe the snow anisotropic reflectance measurements taken at Dome C.

3. HDRF measurements at Dome C

The following sub-sections provide details on the design of GRASS and the HDRF measurements taken using the instrument, including a description of the measurement site.

3.1. HDRF measurement location

Dome C hosts a joint French-Italian research base, located at 75° 06′S and 123° 23′E, and an elevation of 3233 m. The location of Dome C, high on the Antarctic plateau, results in relatively low wind speeds, clear skies and small relief surfaces, which make it an ideal place as a remote sensing calibration site. Unfortunately this study experienced unusually poor weather conditions during the measurement period with frequent cloudy skies and high winds. Consequently, far fewer measurements were taken than planned.

Measurements of HDRF were collected along a linear transect that was both representative of the snowpack around the Dome C area and just east of the tower used by Hudson et al. (2006). The location of the transect, situated nearby the "access" road to the tower, and partially dictated by electricity constraints, may allow future studies to repeat the measurements presented here

6

for comparison before considering other sites in the Dome C area. Eight snow surface sites were studied over the ∼100 m transect depicted in Figure 3. The measurement location showed very few sastrugi and most surface features were small (approximately ∼10 cm scale), which is characteristic of the region. To the authors knowledge there had been no recent (<1 year) anthropogenic ground disturbance in the measurement area, and previous studies have demonstrated that disturbed snow from station construction is buried (Warren et al., 2006).

3.2. Snow pits

At each of the eight measurement sites along the transect a 1 m deep snow pit was dug after recording the radiometric field measurements. Snow density, temperature, grain size, grain type, and penetration profiles were taken down the pit wall. Temperature was recorded every 10 cm through the pit by inserting a thermocouple into the snow, additionally snow density was recorded every 5 cm through weighing a block of snow of known volume (270 cm^3) cut from the wall. Grain size, grain type and snow penetration were all recorded according to the international classification for seasonal snow on the ground (Fierz et al., 2009). The snow grain size was measured by taking a sample of the snow from the pit wall every 10 cm or where a clear change in snow strata was observed. The sample was placed on a 1 mm^2 gridded card and typical grain size was recorded through examination of the snow grains through a hand lens. Owing to the nature of the method used a precise grain size value cannot be obtained but the grain size is instead roughly characterised according to (Fierz et al., 2009) as very fine (<0.2 mm), fine (0.2–0.5 mm), medium (0.5–1.0 mm), coarse (1.0–2.0 mm), very coarse (2.0–5.0 mm) or extreme (>5.0 mm). More detailed stratigraphy of the surface of Dome C snow is available in Gallet et al. (2011).

3.3. GRASS equipment design

GRASS, displayed in Figure 1, consists of a hemispherical frame of 2 m radius, which can be lifted and moved over a target surface (Pegrum et al., 2006). The frame can be rotated on a lower base ring, that is aligned with the sun

at the start of measurements and kept in the same position throughout each measurement sequence. The hemispherical frame consists of an upper base ring that slots into the lower base. Attached to the upper base, arms, spaced at $30°$ increments, run vertically to the apex of the hemisphere. Four radiance collectors are attached to each of these arms positioned at viewing angles of 15, 30, 45 and $60°$ to measure surface radiance. The radiance collectors all point at the centre of the target surface. A further radiance collector is attached at the apex of GRASS facing downwards for measuring surface radiance at nadir ($0°$). Each radiance collector is attached to a fibre optic and has an $8°$ full cone of acceptance. The viewing footprint of each radiance collector ranges from 0.049 m^2 at nadir to 0.142 m^2 at a viewing angle of $60°$; eccentricity of the field of view increases as the viewing angle increases. A further fibre optic is coupled to an integrating sphere, positioned at the top of the GRASS hemisphere to measure the downwelling solar irradiance, as shown in Figure 1. Four additional arms provide support to keep the hemispherical shape and ensure the radiance collectors all point at the same target area. The arms and upper base ring of GRASS can be rotated $360°$ azimuthally enabling surface radiance measurements at a full range of azimuth angles. The fibre optics from the radiance collectors and from the integrating sphere are connected to a visible and shortwave infra-red (VSWIR) spectrometer through a fibre optic multiplexer. Measurements are performed with a $\sim$1 nm spectral resolution in the 400–1700 nm interval.

3.4. Acquiring HDRF measurements with GRASS

3.4.1. Raw measurement collection

Each HDRF characterisation of a target surface through GRASS entailed measurements of surface radiance at twelve azimuth angles, $\sim$30$°$ apart, achieved by rotating the upper ring of GRASS by three turns of $\sim$90$°$. At each azimuth angle surface radiance measurements were taken at four viewing angles ($\theta =$15$°$, 30$°$, 45$°$, 60$°$); leading to a total of 49 azimuth and viewing angle combinations including a surface radiance measurement at nadir ($0°$). The downward irradiance was measured simultaneously to each upwelling surface radiance mea-

8

surement. When rotating the GRASS structure, care was taken to ensure that no part of the structure created a direct shadow over the measurement area. GRASS was therefore not always rotated exactly 90°, but within 80–100°.

Following a complete hemisphere of surface radiance measurements (three rotations of GRASS) a $\sim$0.25 m^2 calibrated Spectralon panel was placed on the target surface and the surface radiance from the panel was recorded with the nadir radiance collector. The radiance measurements from the Spectralon panel provide a reference measurement to which the surface radiance measurements from the target surface can be compared to in order to derive HDRF values, as described in section 3.4.2.

The intensity response of each radiance collector was intercalibrated with each other at the end of each measurement sequence by placing each radiance collector in an integrating sphere illuminated by a stable tungsten-halogen lamp, providing a constant radiance source. The calibration was performed in ambient cold conditions with GRASS in place. Section 3.4.2 describes how these intercalibration values are used in derivation of HDRF values.

Obtaining surface radiance measurements from the whole downwelling hemisphere, the Spectralon panel reference measurement and the radiance collector intercalibration took 2–3 hours for each site. Measurements were only taken within four hours of solar noon when solar zenith angle was highest and the change in its value with time was smallest. Solar zenith angles varied by less than 3.5° over the course of each measurement sequence. The average solar zenith angle for all HDRF measurement sequences was 58.2±5.9°(1SD).

3.4.2. Raw measurement processing to generate HDRF plots

The following procedure was used to derive values of HDRF from surface radiances. Firstly, raw surface radiance values from each radiance collector, $\Phi_{raw}(\theta_r, \phi_r)$, were corrected to determine, $\Phi_{cor}(\theta_r, \phi_r)$, accounting for variation in the response of each individual radiance collector by multiplying Φ_{raw} by a ratio, $\frac{\overline{\Phi_i^{cal}}}{\Phi_i^{cal}}$, between the average radiance of the tungsten-halogen calibration lamp for all radiance collectors, $\overline{\Phi_i^{cal}}$, and the radiance value for a specific

9

radiance collector Φ_i^{cal}; equation 3.

$$\Phi_{cor}(\theta_r, \phi_r) = \left(\frac{\overline{\Phi_i^{cal}}}{\Phi_i^{cal}} \right) \Phi_{raw}(\theta_r, \phi_r) \tag{3}$$

$HDRF(\theta_r, \phi_r)$ is determined using Equation 4, where $E(\theta_r, \phi_r)$ indicates the downwelling irradiance measured at the same time as $\Phi_{raw}(\theta_r, \phi_r)$, and E^{id} indicates the downwelling irradiance recorded while measuring the radiance from the Spectralon reference panel; Φ_{raw}^{id}.

$$HDRF(\theta_r, \phi_r) = \frac{\left(\frac{\Phi_{cor}(\theta_r, \phi_r)}{E(\theta_r, \phi_r)} \right)}{\left(\frac{\Phi_{cor}^{id}}{E^{id}} \right)} = \frac{E^{id}}{E(\theta_r, \phi_r)} \frac{\Phi_{cor}(\theta_r, \phi_r)}{\Phi_{cor}^{id}} \tag{4}$$

Application of equations 3 and 4 to raw surface radiance measurements from GRASS allow for the determination of HDRF values over π steradians, centred on the nadir, with 30° azimuth intervals and 15° viewing increments. The values of HDRF are presented through polar plots. The radius of the plot represents increasing viewing angle (the centre of the plot being 0° and the edge 60°) and the circumference of the plot represents the azimuth angle increasing clockwise.

4. Results

Polar plots of HDRF, determined from details provided in section 3.4.2, are presented in section 4.1. The HDRF polar plot determined by averaging the HDRF plots from individual sites is presented in section 4.2.

4.1. Variation in polar plots of HDRF of individual sites

Figure 4 shows polar plots of HDRF for four representative sites along the 100 m transect at a wavelength of 1000 nm with snow pit data and a photo of the snow surface for the four representative sites. The variation in HDRF at nadir with wavelength is also shown and a description of the snow topography for each site is included with the average solar zenith angle during measurement of HDRF. Snow topography is considered as small scale inhomogeneities of the snow surface will affect the HDRF especially with the relatively small viewing

10

footprint of GRASS. Knowledge of snow physical properties below the measurement site is critical because it affects radiative transfer of light in the snowpack and consequently affects HDRF. The e-folding depths (a metric for light penetration) at 400 nm were ~10 cm for the windpack layers and ~20 cm for the hoar-like layer. At 600 nm e-folding depths decreased to ~8 cm for the wind-packed snow and to ~5 cm for the hoar-like snow. Snow is optically thick after 3–4 e-folding depths (France et al., 2011), thus the structure of snow may affect the surface reflectance up to a depth of ~80 cm. France et al. (2011) described the stratigraphy of the top 80 cm of Dome C snow as generally consisting of a surface windpack and a hoar-like layer beneath the windpack.

Two features are apparent from the typical HDRF plots presented in figure 4. Firstly there is significant variation in the shape of the plots between sites showing that small spatial (<<1m) heterogeneity occurs in Dome C HDRF measurements. Secondly the shape of individual plots deviates from symmetrical across the solar principal plane; Warren et al. (1998) state several causes of variation in snow anisotropic reflectance measurements, including solar zenith angle, snow properties including grain size, grain shape and snow topography. The measurements at the four sites were taken under similar solar zenith angles ranging from 52.3 to 63.9°, therefore differences in the polar plots which occur between the sites are most likely to be due to small scale differences in snow stratigraphy and topography. Along the transect, different snow features and snow types were encountered as seen in figure 4, which were representative of the Dome C area.

The surface snow grain size at each site was very similar, being either "fine" (0.2–0.5 mm) or "very fine" (<0.2 mm). At all sites, at the base of the snow profiles a coarse-grained (>5 mm) depth hoar was found which began at depths ranging from ~30 cm, at site B, to ~60 cm for site C. The top 10 cm surface layer of snow were characterised by fine, rounded-faceted grains mixed with rounded grains at sites B, C and D, and just rounded-faceted grains at site A. The penetrability of the surface layer ranged between sites from hard to very soft. The hardest surface occurs at sites A and B while the softest surface occurs

11

at site C. It is difficult to correlate the different polar plots of HDRF observed with particular snow features but it appears that the snow topography may be the dominant controlling factor on the shape of the HDRF plots.

The site descriptions and the snow surface photos give an indication of snow topography for each measurement location. Inhomogeneities in snow topography across a measured snow surface could result in the non-symmetrical plots observed in figure 4. The snow surfaces observed at Dome C range from smooth (to the eye) to having small scale (cm scale) ripples or rough surfaces. Sites B and C exhibit smooth surfaces, and also exhibit the strongest HDRF forward scattering pattern and the most symmetrical plots. The snow surfaces of sites A and D showed rougher topography. Site A had a slightly rippled snow surface, consequently the polar plot of site A exhibits lower HDRF values around azimuth values of $0°$; showing the snow is less forward scattering. Site D had a rough surface with a raised area of snow covering about a quarter of the measurement area which may cause the asymmetrical plot observed. The decrease in snow anisotropy with increased surface roughness was also noted by Hudson et al. (2006).

Although there are differences between the polar plots for individual sites, similarities can be drawn. All the polar plots of HDRF in Figure 4 show the snow is forward scattering with values peaking at the top of the plots, in agreement with Kuhn (1985); Dozier et al. (1988); Warren et al. (1998); Leroux et al. (1999); Aoki & Fukabori (2000); Painter & Dozier (2004); Li & Zhou (2004); Peltoniemi et al. (2005); Dumont et al. (2010). The forward scattering pattern is most clear in sites B, C and D where the forward scattering peak occurs at zenith angles $>55°$ and azimuth angles $\pm 45°$ of $0°$. Values of HDRF are also generally similar between sites compared to variation seen for other Earth surfaces, for example, grass, trees and water (e.g. Sandmeier et al. (1998); Voss et al. (2007); Sayer et al. (2010)), with most values ranging from 0.8–1.1. Finally, the spectral values of HDRF at nadir displayed in Figure 4 exhibit features consistent with reflectance spectra of deep snow packs characterised by small grain size (Choudhury & Chang, 1981; Dozier et al., 1988; Zibordi et al.,

12

1996). This further confirms that the differences in HDRF values among sites A–D are mostly explained by small scale topographic features.

Figure 5 shows the variation in HDRF for all eight sites along the solar principle plane at wavelengths of 400, 600, 800, 1000, 1200, 1400 and 1600 nm. Site descriptions of the four extra sites not represented in figure 4 (sites E, F, G and H) are provided in the caption of figure 5. Graphs in figure 5 almost systematically exhibit a forward scattering peak at large positive viewing angles. Smoother snow surfaces typically show a smoother variation in HDRF with viewing angle and a more pronounced forward scattering peak. Variation in HDRF as a function of viewing angle also becomes smoother as wavelength increases due to both a decreasing influence of diffuse radiation over direct radiation and an increase in ice absorption efficiency resulting in fewer scattering events, leading to less randomisation in photons direction with increasing wavelength. As wavelength increases to over 800 nm the values of HDRF approximate to BRF value. Figure 5 clearly shows the decrease in snow HDRF with increasing wavelength, as would be expected for snow surfaces.

4.2. A spatially averaged HDRF polar contour plot of a Dome C snow surface

The polar plots shown in figure 4 clearly show differences in small scale (<<1 m) HDRF measurements. Thus, this paper provides representative measurements of small scale HDRF, useful for radiative-transfer models and potential importance for future high resolution (<1 m) satellite sensors (Jacobsen, 2005).

For the HDRF reported here to be applicable for calibration of typical current satellite sensors (with a GSD of ∼10 m to 100 m) an HDRF distribution can be created by spatially averaging the polar plots of individual sites and compared to the results from Hudson et al. (2006), who measured anisotropic reflectance of Dome C snow surfaces from the top of a 32 m tower and thus had a much larger viewing footprint (70 m^2 at viewing angles of 22.5° up to 1170 m^2 at 82.5°) which averaged over any local surface inhomogeneities.

13

Hudson et al. (2006) reflect their polar plots assuming that values are symmetrical across the solar principle plane. To compare the results presented here to those measured by Hudson et al. (2006) the HDRF is symmetrised across the solar principle plane. To achieve this a spatially averaged value of HDRF at a known azimuth and viewing angle on one side of the solar principle plane is averaged with the corresponding HDRF on the other side of the solar principle plane.

Average HDRF polar plots at 400, 600, 800, 1000, 1200, 1400 and 1600 nm are shown in Figure 6. The average solar zenith angle was $52.8\pm5.9°$(1SD). The snow surface is markedly forward scattering at all wavelengths with a very similar HDRF pattern in the 400–800 nm spectral interval. A marked decrease in the values of HDRF occurs beyond 800 nm with the value of the prominent forward scattering peak, decreasing from ∼1.05 at 600 nm down to ∼0.25 at 1600 nm. Therefore showing an expected decrease in reflectance with wavelength. However the relative change in HDRF with azimuth and viewing angle becomes larger with wavelength. Specifically, at 600 nm the HDRF peak is 1.1 times the value at nadir while at 1600 nm it is 1.67 times. The HDRF forward scattering pattern remains constant with wavelength and occurs at $\pm60°$ of the solar principal plane and at a viewing angle of ∼60°. Although there is a clear forward scattering peak observed, the whole of this peak cannot be observed. Viewing angles larger than 60° are not reported as the optics would be observing the base ring of GRASS.

In agreement with literature results, HDRF presented in Figure 6 confirm that: (i.) snow is forward scattering; (ii.) the forward scattering increases with wavelength; (iii.) reflectance decreases with wavelength. Section 5 will investigate further agreement between the measurements presented in this study and those from Hudson et al. (2006).

5. Discussion

The discussion will compare the HDRF data from this study with those derived from data published by Hudson et al. (2006). The section will also discuss the accuracy of data produced by GRASS.

5.1. Comparison to previous Dome C measurements

Hudson et al. (2006) measured the anisotropic reflectance of Dome C surfaces in the form of an "anisotropic reflectance factor" at wavelengths 350–2400 nm. The measurement method of Hudson et al. (2006) varies from that presented here as GRASS includes all azimuth angles in one measurement sequence. GRASS also observes the same snow surface at each azimuth/viewing angle, within the limits of the varying small sensor footprint. The measurements made with GRASS have a much smaller footprint than the measurements by Hudson et al. (2006), with the GRASS measurement footprints varying from 0.049 m^2 at nadir to 0.142 m^2 at a viewing angle of 60° and the footprint of the measurements of Hudson et al. (2006) varying from 70 to 1170 m^2. The smaller footprint of the measurements made by GRASS means that each measurement is only representative of a relatively small snow surface measured. However, the representative HDRF contour plots of figure 6 are comparable with the anisotropic reflectance factor measurements of Hudson et al. (2006). For comparison purposes, the anisotropic reflectance factor values, ψ, presented by Hudson et al. (2006) are converted to HDRF values, using equation 5, where α is albedo.

$$HDRF = \psi\alpha \tag{5}$$

Figure 7 shows a comparison of a BRF polar contour plot at 1000 nm from Hudson et al. (2006) to the equivalent HDRF determined from GRASS. Underneath each of these polar plots is the variation in HDRF along the solar principle plane for the GRASS and Hudson et al. (2006) data sets. Data at wavelengths of 400, 600, 800, 1000, 1200, 1400 and 1600 nm is shown. The

anisotropic reflectance factor data from Hudson et al. (2006) are for a solar zenith angle of 58.2°, which is effectively the same as the average solar zenith angle for which the HDRF measurements with GRASS were taken. The albedo measurements are from Hudson et al. (2006) figure 6. Note, the polar contour plots only display HDRF values for viewing angles measured by Hudson et al. (2006) that are similar to those measured by GRASS for comparative purposes. Figure 7 also shows the absolute difference between the GRASS measurements and the Hudson et al. (2006) measurements ($HDRF_{Hudson} - HDRF_{GRASS}$) both for the polar plots and the variation across the solar principle plane at different wavelengths. For the polar contour plots, at a wavelength of 1000 nm, the agreement between Hudson et al. (2006) and the work presented here is very good, with 95% of the viewing and azimuth angles compared exhibiting less than 4% relative difference ($\frac{HDRF_{GRASS}}{HDRF_{Hudson}} \times 100$) . The best agreement occurs at smaller viewing angles where the difference is less than 2%. The agreement is less good at some higher viewing angles, particularly in the backwards scattering direction (at the base of the plot) where the difference is around 6%. An effect which is also clearly seen in the change of values across the solar principle plane. Both the measurements from GRASS and Hudson et al. (2006) show the snow is forward scattering, peaking in the forwards direction around values of 0.8 at a wavelength of 1000 nm. The shape of the polar contour plot is very similar, with the forward peak occurring at similar azimuth angles, although over a slightly greater range in Hudson et al. (2006). Both GRASS and Hudson et al. (2006) indicate a slight backscattering. The variation in HDRF across the solar principle plane between Hudson et al. (2006) and GRASS measurements is very similar at all wavelengths. The agreement is weaker at the shortest wavelengths (400–800 nm) where the influence of diffuse radiation is the greatest. There appears to be an overall trend that the Hudson et al. (2006) values are slightly larger (from 0 to 0.1) than the GRASS values for shorter wavelengths and smaller than the GRASS values for longer wavelengths, although the difference at all wavelengths is still relatively small ($\sim \pm 0.05$). Figure 7 suggests that even though GRASS provides a very different method to that utilised by Hud-

16

son et al. (2006) the results produced are very similar, adding strength to both the data presented here and those presented by Hudson et al. (2006). Thus, supporting the use of both data sets for current satellite inter-calibration and inter-comparison activities.

5.2. Uncertainty of HDRF measurements using GRASS

Sandmeier (2000) reviewed uncertainties in BRDF (HDRF) measurements from field goniometers and how these sources of uncertainties are best reduced. Sources of uncertainty include geometrical accuracy of the goniometer, atmospheric conditions and the reflectance properties of the Spectralon reference panel. Section 5.2 will ascertain how each of these uncertainties could have impacted the HDRF results presented here.

5.2.1. Geometrical accuracy

The geometrical accuracy of the goniometer defines measurement repeatability (Sandmeier, 2000). For geometrically accurate HDRF measurements the centre of a viewing footprint of a radiance collector should always point at the centre of the target (Sandmeier, 2000). In the case of GRASS, the centre of the viewing footprint for the nadir fibre radiance collector as it is rotated into the four 90° apart positions deviates from the centre of the hemisphere surface by an average of 6.7 cm. All radiance collectors on GRASS centre on the same target surface within the viewing footprint. To test the repeatability of GRASS, HDRF measurements of a white linoleum surface were repeated six times with constant illumination provided by tungsten-halogen lamps placed at a zenith angle of 50°. Repeatability tests performed under very stable laboratory conditions indicated relative uncertainty was achieved of 5% (see (Ball et al., 2014 In Press)). Clearly, these values are expected to largely increase with natural targets exhibiting large surface inhomogeneities.

5.2.2. Atmospheric conditions

Atmospheric conditions can influence reflectance measurements. In order to minimise their effects, measurements were only taken in clear sky conditions,

17

or when there was only a very small amount of cloud low at the horizon. Atmospheric column aerosol at Dome C is minimal. Aerosol optical thickness was measured during field measurements with a Microtops Sunphotometer, with average values of $\sim$0.04 (1 SD) at 440 nm. These values are slightly higher than the average values recorded at Dome C by Six et al. (2005) of 0.02 at 440 nm likely explained by uncertainties in the absolute calibration of sun-photometers.

Variability in downwelling irradiance was recorded during each measurement sequence through the calibrated integrating sphere which recorded downwelling irradiance near-simultaneously to each surface radiance measurement. Downwelling irradiance typically varied by less than 3% during the course of a measurement sequence and variation in downwelling irradiance is accounted for in the data analysis.

5.2.3. Spectralon reference panels

The Spectralon reference panel used to calculate HDRF is assumed to be a perfect Lambertian reflector, however several studies (e.g. Kimes & Kirchner (1982); Jackson et al. (1992); Sandmeier et al. (1998)) demonstrate deviations up to 8% from Lambertian (Sandmeier et al., 1998). In the measurements presented here the reflectance of the reference panel is only measured at the nadir, still the non-ideal Lambertian reflectance of the reference panel may affect the determination of E^{id} as a function of the sun-zenith angle. The panel was spectrally and angularly calibrated at the National Physical Laboratory prior to the measurements by GRASS and was shown to deviate by up to 2% from Lambertian over wavelengths of 450 to 1000 nm and at the nadir viewing angle under the illumination zenith angles observed in this study (52–64°). This deviation of the Spectralon panel from Lambertian is not specifically accounted for in the data analysis. Spectralon panels are typically calibrated at room temperature, Ball et al. (2013) showed there was no significant difference between measurements taken at room temperature ($\sim$20°C) and at a polar temperatures despite a phase transition in the panels at 19°C.

6. Conclusions

HDRF of snow surfaces were determined from measurements made at eight sites along a ∼100 m transect at Dome C, Antarctica, using the gonio-radiometric spectrometer system (GRASS). These data complement previous observations performed at Dome C in the same location using a significantly different method and scale. Consistent with previous studies the HDRF results from GRASS show the marked forward scattering of snow. Polar plots of HDRF from the individual measurement sites show slight differences in the HDRF patterns, which is likely to be due to snow surface features or snow properties. The variation in HDRF caused by small scale (<<1 m) heterogeneity was not previously examined at Dome C. Small scale heterogeneity is important for potential future high resolution satellite sensors. To represent a more typical current satellite viewing footprint (10–100 m) a HDRF polar plot representative for Dome C was created by averaging the HDRF values from the eight different sites over the 100 m transect. Results from the spatially averaged HDRF plots indicate that as wavelength increases, the prominence of the forward scattering increases, although overall reflectance decreases. The plots also show very good agreement with previous Dome C measurements. At a wavelength of 1000 nm the absolute difference in HDRF ranged from 0±0.04, which equates to the values of Hudson et al. (2006) being up to 5% different compared to the GRASS values, with 80% of all values at 4% difference or below, even though the techniques utilised to measure HDRF are significantly different. The results presented here strengthen the confidence on current Dome C measurements for the inter-calibration and inter-comparison of satellite optical data.

19

Angal, A., Chnader, G., Xiong, X., Choi, T., & Wu, A. (2011). Characterisation of the Sonoran desert as a radiometric calibration target for Earth observing sensors. *Journal of Applied Remote sensing*, *5*.

Aoki, T., & Fukabori, M. (2000). Effects of snow physical parameters on spectral albedo and bidirectional reflectance of snow surface. *Journal of Geophysical Research*, *105*, 10,219–10,236.

Ball, C., Levick, A., Woolliams, E., Green, P., Dury, M., Winkler, R., Deadman, A., Fox, N., & King, M. (2013). Effect of polytetrafluoroethylene (PTFE) phase transition at 19 °C on the use of Spectralon as a reference standard for reflectance. *Applied Optics*, *52*, 4806–4812.

Ball, C., Marks, A., Green, P., MacArthur, A., Maturilli, M., Fox, N., & King, M. (2014 In Press). Hemispherical-directional reflectance of windblow snow-covered arctic tundra at large solar zenith angles. *Transactions on Geoscience and Remote Sensing*, .

Choudhury, B., & Chang, A. (1981). On the angular variation of solar reflectance of snow. *Journal of Geophysical Research*, *86*, 465–472.

Dozier, J., Davis, R., Chang, A., & Brown, K. (1988). The spectral bidirectional reflectance of snow. In T. Guyenne, & J. Hunt (Eds.), *Spectral Signatures of Objects in Remote Sensing, Proceedings of the conference held 18-22 January, 1988 in Aussois (Modane), France* (p. 87).

Dumont, M., Brissaud, O., Picard, G., Schmitt, B., Gallet, J., & Arnaud, Y. (2010). High-accuracy measurements of snow bidirectional reflectance distribution function at visible and nir wavelengths-comparison with modelling results. *Atmospheric Chemistry and Physics*, *10*, 2507–2520.

Fierz, C., Armstrong, R., Durand, Y., Etchevers, P., Greene, E., McClung, D., Nishimura, K., Satyawali, P., & Sokratov, S. (2009). *The International Classification of Seasonal Snow on the Ground*. ICSI-UCCS-IACS Working Group on Snow Classification.

Fox, N., Kaiser-Weiss, A., Schmutz, W., Thome, K., Young, D., Wielicki, B., Winkler, R., & Woolliams, E. (2011). Accurate radiometry from space: an essential tool for climate studies. *Philosophical Transactions of The Royal Society A*, *369*.

France, J., King, M., Frey, M., Erbland, J., Picard, G., Preunkert, S., MacArthur, A., & Savarino, J. (2011). Snow optical properties at Dome C (Concordia), Antarctica; implications for snow emissions and snow chemistry of reactive nitrogen. *Atmospheric Chemistry and Physics*, *11*, 9787–9801.

Gallet, J., Domine, F., Arnaud, L., Picard, G., & Savarino, J. (2011). Vertical profiles of the specific surface area and density of the snow at Dome C and on a transect to Dumont D'Urville, Antarctica – albedo calculations and comparison to remote sensing products. *The Cryosphere*, *5*, 631–649.

Hudson, S., Warren, S., Brandt, R., Grenfell, T., & Six, D. (2006). Spectral bidirectional reflectance of Antarctic snow: Measurements and parameterization. *Journal of Geophysical Research*, *111*, 106.

Jackson, R., Clarke, T., & Moran, M. (1992). Bidirectional calibration results for 11 spectralon and 16 $BaSO_4$ reference reflectance panels. *Remote Sensing of Environment*, *40*, 231–239.

Jacobsen, K. (2005). High Resolution Imaging Satellite Systems. In *3D Remote Sensing Workshops*. European Association of Remote Sensing Laboratories.

Keller, L., G., W., C., S., M., W., & R., H. (2002). Antarctic automatic weather station data for the calendar year 1998. Madison, WI, University of Wisconsin-Madison, Space Science and Engineering Center, 2002. Call Number: UW SSEC Publication No.02.07.K1.

Kiehl, J., & Trenberth, K. (1997). Earth's annual global mean energy budget. *Bulletin of the American Meteorological Society*, *78*, 197–208.

Kimes, D., & Kirchner, J. (1982). Irradiance measurement errors due to the assumption of a lambertian reference panel. *Remote Sensing of Environment*, *12*, 141–149.

Kuhn, M. (1985). Bidirectional reflectance of polar and alpine snow surfaces. *Annals of Glaciology*, *6*, 164–167.

Leroux, C., Lenoble, J., Brogniez, G., Hovenier, J., & Haan, J. D. (1999). A model for the bidirectional polarized reflectance of snow. *Journal of Quantitative Spectroscopy and Radiative Transfer*, *61*, 273–285.

Li, S., & Zhou, X. (2004). Modelling and measuring the spectral bidirectional reflectance factor of snow-covered sea ice: an intercomparison study. *Hydrol Process*, *18*, 3559–3581.

Masonis, S., & Warren, S. (2001). Gain of the AVHRR visible channel as tracked using bidirectional reflectance of Antarctic and Greenland snow. *International Journal of Remote Sensing*, *22*, 1495–1520.

Middleton, W., & Mungal, A. (1952). The luminous directional reflectance of snow. *Journal of the Optic Society of America*, *42*.

Nicodemus, F., Richmond, J., Hsia, J., Ginsberg, I., & Limperis, T. (1977). Geometrical considerations and nomenclature for reflectance. *U.S. Department of commerce, National Bureau of Standards*, .

Painter, T., & Dozier, J. (2004). The effect of anisotropic reflectance on imaging spectroscopy of snow properties. *Remote Sensing of Environment*, *89*, 409–422. doi:10.1016/j.rse.2003.09.007.

Pegrum, H., Fox, N., Chapman, M., & Milton, E. (2006). Design and testing a new instrument to measure the angular reflectance of terrestrial surfaces. In *IEEE International Conference on Geoscience and Remote Sensing Symposium, 2006. IGARSS 2006.* (pp. 1119–1122).

22

Peltoniemi, J., Kaasalainen, S., Naranen, J., Matikainen, L., & Piironen, J. (2005). Measurement of directional and spectral signatures of light reflectance by snow. *IEE Transactions on Geoscience and Remote Sensing*, *43*, 2294–2304. doi:10.1109/TGRS.2005.855131.

Petit, J., Jouzel, J., Pourchet, M., & Merlivat, L. (1982). A detailed study of snow accumulation and stable isotope content in Dome C (Antarctica). *Journal of Geophysical Research*, *87*, 4301–4308.

Rémy, F., Shaeffer, P., & Legrésy, B. (1999). Ice flow physical processes derived from the ERS-1 high-resolution map of the Antarctica and Greenland ice sheets. *Geophysical Journal International*, *139*, 645–656.

Sandmeier, S. (2000). Acquisition of bidirectional reflectance factor data with field goniometers. *Remote Sensing of Environment*, *73*, 257–269.

Sandmeier, S., Müller, C., Hosgood, B., & Andreoli, G. (1998). Sensitivity Analysis and Quality Assessment of Laboratory BRDF Data. *Remote Sensing of Environment*, *64*, 176–191.

Sayer, A., Thomas, G., & Grainger, R. (2010). A sea surface reflectance model for (A)ATSR and application to aerosol retrievals. *Atmospheric Measurement Techniques*, *3*, 813–838.

Schaepman-Strub, G., Schaepman, M., Painter, T., Dangel, S., & Martonchik, J. (2006). Reflectance quantities in optical remote sensing–definitions and case studies. *Remote Sensing of Environment*, *103*, 27–42.

Six, D., Fily, M., Alvain, S., Henry, P., & Benoist, J. (2004). Surface characterisation of the Dome Concordia area (Antarctica) as a potential satellite calibration site, using Spot 4/Vegetation instrument. *Remote Sensing of Environment*, *89*, 83–94.

Six, D., Fily, M., Blarel, L., & Goloub, P. (2005). First aerosol optical thickness measurements at dome c (east antarctica), summer season 2003–2004. *Atmospheric Environment*, *39*, 5041–5050.

23

Trenberth, K., Fasullo, J., & Kiehl, J. (2009). Earth's global energy budget. *American Meteorological Society*, *90*.

620 Voss, K., Morel, A., & Antoine, D. (2007). Detailed validation of the bidirectional effect in various case 1 waters for application to ocean color imagery. *Biogeosciences*, *4*, 781–789.

Warren, S. (1982). Optical properties of snow. *Reviews of geophysics and space physics*, *20*, 67–89.

625 Warren, S., Brandt, R., & Grenfell, T. (2006). Visible and near-ultraviolet absorption spectrum of ice from transmission of solar radiation into snow. *Applied Optics*, *45*, 5320–5334.

Warren, S., Brandt, R., & Hinton, P. (1998). Effect of surface roughness on bidirectional reflectance of Antarctic snow. *Journal of Geophysical Research*,
630 *103*, 25.

Zibordi, G., Meloni, G., & Frezzotti, M. (1996). Snow and ice reflectance spectra of the Nansen Ice Sheet surfaces. *Cold regions science and technology*, *24*, 147–151.
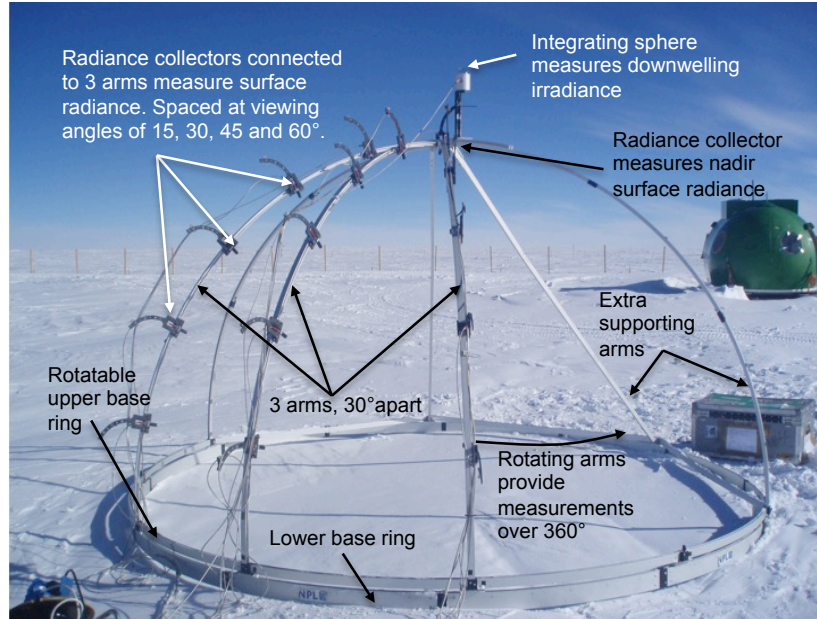
8. Figures

Figure 1: A picture of GRASS: radiance collectors are attached to three arms spaced 15° apart, a radiance collector is attached at nadir to record surface radiance. On top of the structure there is an integrating sphere to measure downwelling irradiance. The radiance collectors are connected to the spectrometer via fibre optics. The arms of GRASS can be rotated 360° to record surface radiance at all azimuth angles.
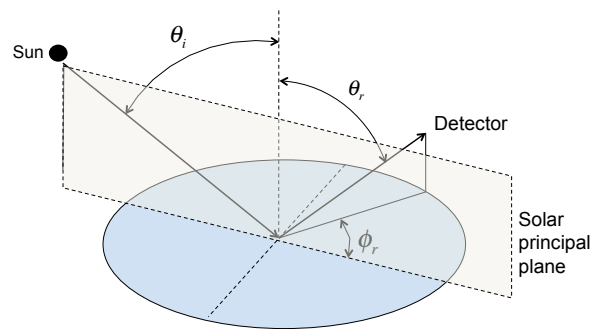

Figure 2: Definition of angles required for BRDF measurements, θ_i is the zenith angle of incidence light, ϕ_r is the azimuth angle and θ_r is the viewing angle. Azimuth angles are measured relative to the solar principle plane.

Figure 3: Location of ∼100 m transect over which GRASS measurements were taken. The transect runs parallel to a little used access "road" running from the main base to the "American tower" from which this photo was taken. The recent disturbed snow was due to tracked vehicles moving GRASS and ancillary equipment into position. To the authors' knowledge this area has had no athropogenic ground disturbance for more than a year.
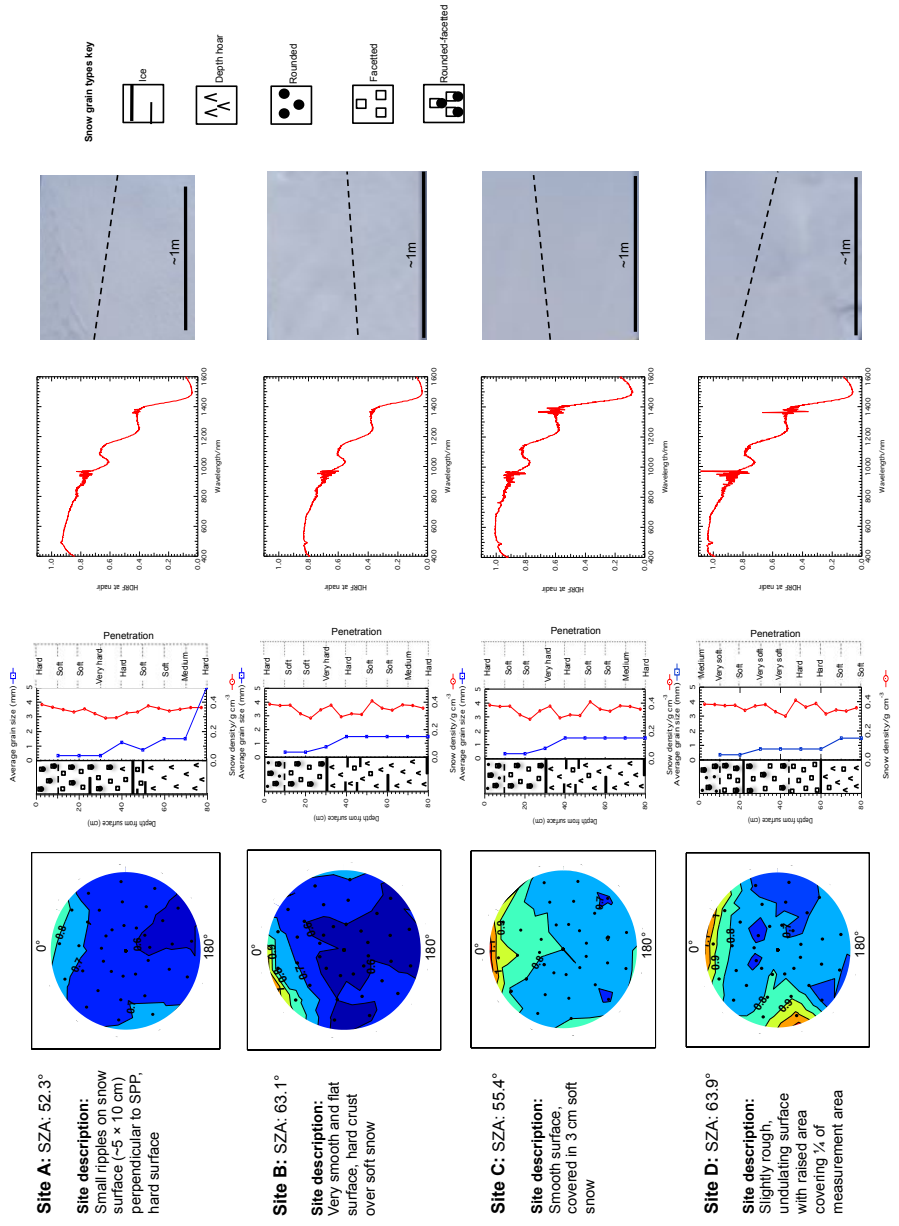
Figure 4: Four typical polar contour plots of HDRF for individual sites along the 100 m transect studied each at a wavelength of 1000 nm. Black dots on the plots show measured azimuth and viewing angles. SPP is the solar principal plane, which runs from the top to bottom (left to right) of each plot with the sun at the base of the plot. Snow pit data from each site is also shown, including snow grain type, size, snow density and penetrability/hardness. Snow is classified according to the classification system of Fierz et al. (2009). For the grain size only its central value is shown, e.g., coarse snow (1.0–2.0 mm), is shown as 1.5 mm, with uncertainty bounded by the classification limits. Spectral variations in HDRF at nadir is shown with a description of each site, a site photo, and the average solar zenith angle (SZA). The solar principle plane is shown on the site photos by a dashed black line.
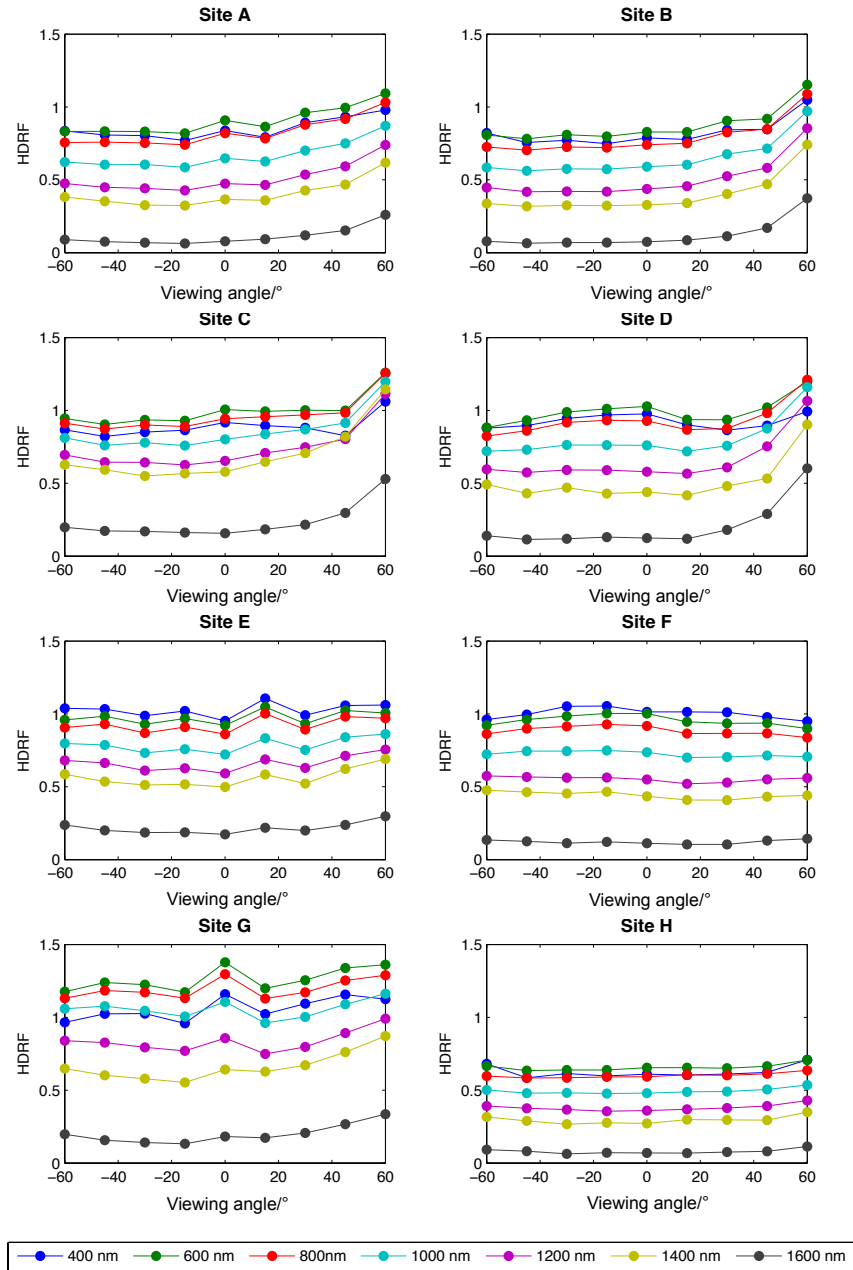
Figure 5: Variation in HDRF across the solar principle plane for wavelengths 400, 600, 800, 1000, 1200, 1400, 1600 and 1800 nm for all eight sites. Positive zenith angles are away from the sun and negative zenith angles are towards the sun. Site descriptions for sites A–D can be found in figure 4. Site E description: Flat surface with a few ripples, soft snow surface. Site F description: Smooth surface with some ripples, hard snow surface. Site G: Snow surface with slight ripples, hard surface. Site H: Smooth, flat surface, hard upper surface.
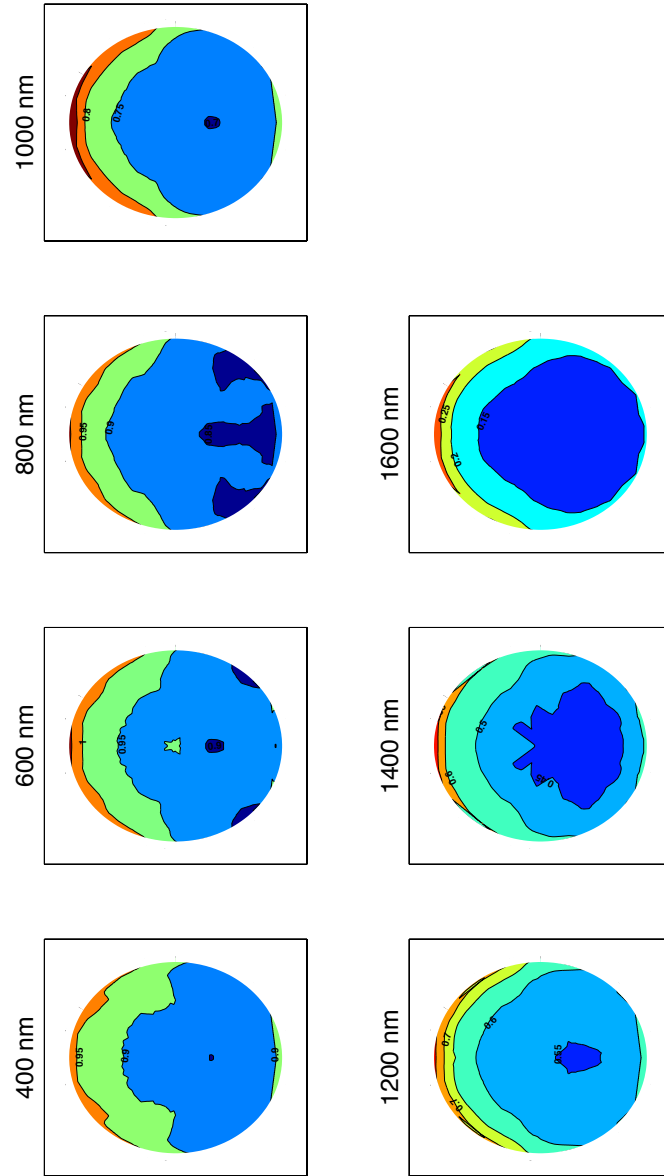
Figure 6: Representative polar plots from HDRF averaged across all 8 sites at wavelengths 400–1600 nm, note that the colour scale is different for each polar plot. Average solar zenith angle was 58.2±5.9° (1SD). The solar principle plane runs vertically from the top to bottom (left to right) of the plots with the top of the plot being 0° of azimuth and the sun is at the base of the plots.
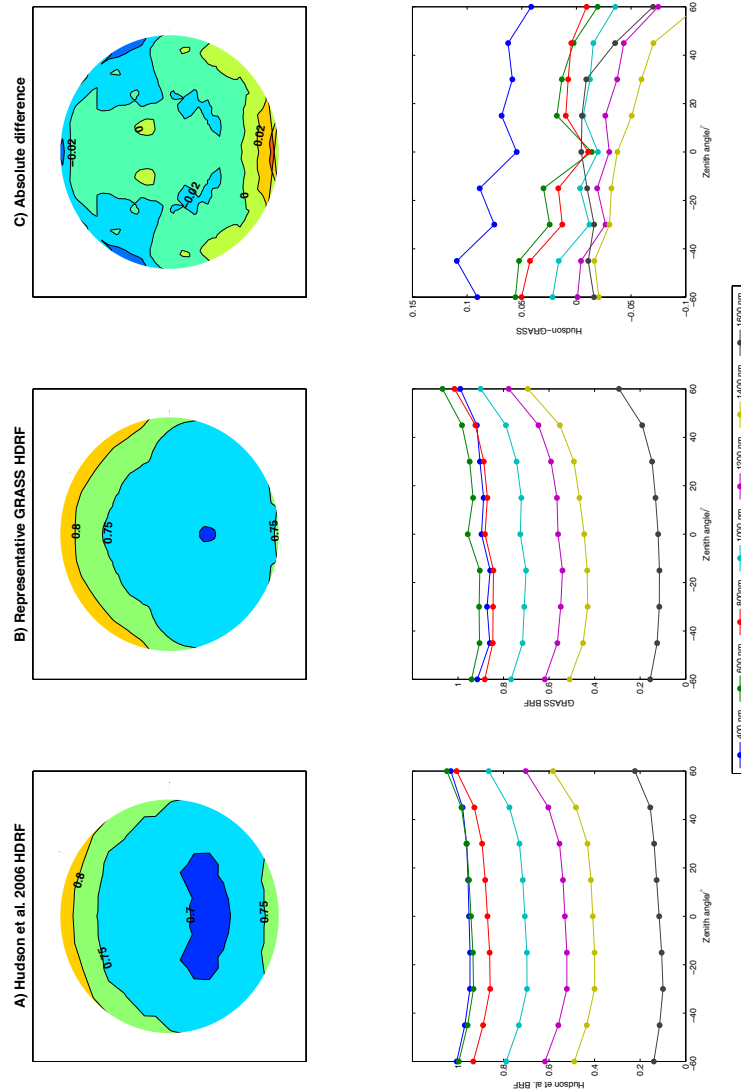
Figure 7: Comparison between HDRF measurements by Hudson et al. (2006) compared to HDRF measurements presented here. Top polar contour plots show variation in the HDRF at 1000 nm. The bottom plots show variation at all various wavelengths across the solar principle plane, and the absolute difference between the GRASS measurements and Hudson et al. (2006) measurements. The solar principle plane runs vertically from the top to bottom (left to right) of the plots.